Chaos
An Interdisciplinary Journal of Nonlinear Science

RESEARCH ARTICLE | MAY 07 2026

General oblique projections for model reduction via spectral submanifolds

Leonardo Bettini ; Amirhossein Kazemipour ; Robert K. Katzschmann ; George Haller

Chaos 36, 053122 (2026)
https://doi.org/10.1063/5.0319241

General oblique projections for model reduction via spectral submanifolds

Cite as: Chaos 36, 053122 (2026); doi: 10.1063/5.0319241
Submitted: 23 December 2025 · Accepted: 20 April 2026 ·
Published Online: 7 May 2026

Leonardo Bettini,[1] Amirhossein Kazemipour,[2] Robert K. Katzschmann,[2] and George Haller[1,a)]

AFFILIATIONS

[1]Institute for Mechanical Systems, ETH Zurich, Leonhardstrasse 21, 8092 Zurich, Switzerland
[2]Soft Robotics Lab, ETH Zurich, Tannenstrasse 3, 8092 Zurich, Switzerland

[a)]**Author to whom correspondence should be addressed:** georgehaller@ethz.ch

ABSTRACT

Slow spectral submanifolds (SSMs) are low-dimensional, attracting, invariant surfaces in the phase space of a dynamical system that carry the dominant nonlinear dynamics. Nearby trajectories rapidly converge to such slow SSMs and synchronize with its internal dynamics thereby enabling mathematically rigorous model reduction to the SSM. In general, oblique projections are required for optimally associating full trajectories off the SSM to their SSM-reduced counterparts. In this work, we establish a rigorous mathematical mapping of the SSM onto its tangent space via general oblique projections and develop a data-driven procedure to efficiently construct SSM-based reduced-order models using these projections. Our approach applies irrespective of the SSM dimension and assumes only limited trajectory information. We illustrate the method on numerical and experimental examples, including nonlinear beam oscillations and artificial muscle actuators.

Data-driven reduced-order modeling attracts growing interest in the analysis and control of nonlinear dynamical systems in various areas of applied science and engineering. Reduction to slow spectral submanifolds (SSMs) provides a mathematically rigorous approach to nonlinear model reduction, as system trajectories rapidly synchronize with the internal dynamics of such slow SSMs. When nonlinear interactions are strong or when the linearized system exhibits pronounced non-normality, accurate parametrization of the SSM and identification of the reduced dynamics on it require oblique projections. Here, we develop a data-driven identification of such oblique projections from a limited amount of experimental data obtained from strongly non-normal and nonlinear systems, applicable irrespective of the SSM dimension and independent of whether the underlying spectral subspace contains oscillatory or non-oscillatory modes.

I. INTRODUCTION

Reduced-order models attract growing interest in the scientific community due to the general need to describe complex nonlinear dynamical systems using low-dimensional equations. Such reduced models have the potential to provide accurate prediction, effective control, and fast parametric analysis, while retaining physical interpretability. Low-dimensional models are particularly helpful when only experimental data are available and analytical models are not within reach. Numerous model reduction techniques seeking to meet this objective have been proposed in recent years (see Benner *et al.*,[1] Rowley and Dawson,[2] Taira *et al.*,[3] Brunton *et al.*,[4] and Ghadami and Epureanu[5] for reviews).

Most contemporary data-driven model reduction schemes for time-varying datasets simply fit a parametrized family of linear or nonlinear dynamical systems to the available data. They do so without exploring and utilizing low-dimensional invariant structures in the phase space of a generic dynamical system that tend to govern the dominant behavior of the system. An exception to this approach is the recently emerged methodology of reduction to spectral submanifolds (SSMs). SSMs are low-dimensional invariant manifolds that are tangent to spectral subspaces of the linear part of a nonlinear system at a fixed point. Slow SSMs are tangent to the low-dimensional spectral subspaces of the same dimension that carry slow stable dynamics along with potential unstable dynamics that the linearized system may have. Such slow SSMs form a continuous family but precisely one member of this family, the primary SSM, is as smooth as the original dynamical system under appropriate nonresonance conditions. The remaining members of

the family, the secondary (or fractional) SSMs, have reduced differentiability at the fixed point (see Haller[6] for a general introduction to the subject).

SSM theory offers a rigorous mathematical generalization of nonlinear normal modes (NNMs), originally introduced in the seminal work of Shaw and Pierre[7,8] and further developed by Shaw *et al.*[9] The mathematical foundation for SSMs in systems with stable hyperbolic fixed points was later established by Cabré *et al.*[10] and Haller and Ponsioen.[11] As trajectories converge to an attracting primary SSM, they synchronize exponentially fast with a specific trajectory on the SSM, making the internal dynamics of the primary SSM a smooth, nonlinear reduced-order model of the full dynamics. Classical linearization theory near hyperbolic fixed points further ensures that off-SSM initial conditions, which converge fastest to a specific on-SSM initial condition, form an $(n-d)$-dimensional surface, where n is the dimension of the full system and d is the dimension of the SSM. This surface is known as the stable fiber whose base point is the on-SSM initial condition just mentioned. Stable fibers have the same smoothness as the full dynamical system and form a smooth foliation in a neighborhood of the SSM. Importantly, this foliation is invariant under the flow map, meaning that stable fibers are mapped into stable fibers by the full flow map (see Wiggins,[12] Szalai,[13,14] and Haller[6] for more discussion), while individual fibers are not invariant.

In data-driven SSM constructions, available trajectories typically evolve from initial conditions located off the primary SSM. For the accurate reconstruction of the SSM-reduced dynamics, it is essential to identify the base points of the stable fibers that contain the initial conditions of the available trajectories. As shown in Bettini *et al.*,[15] if an off-SSM initial condition lies close to a nearly flat SSM and the slow and fast eigenspaces at the fixed point are nearly orthogonal, then a simple orthogonal projection onto the SSM suffices to locate the corresponding on-SSM stable fiber base point. Such an SSM-based orthogonal projection has provided several accurate SSM-reduced order models that have successfully predicted both unforced and forced responses in equation-based and data-driven contexts (see Haller,[6] Haller and Ponsioen,[11] Cenedese *et al.*,[16,17] Axås *et al.*,[18] Cenedese *et al.*,[19] Haller and Kaundinya,[20] and Bettini *et al.*[21]).

In many experiments, however, only a single observable is available, requiring delay embedding for manifold reconstruction (Takens[22]). In such cases, the slow and fast subspaces of the linearized system are typically strongly non-orthogonal in the delay-embedding space. This non-normality is evident in structural vibration data from resonance-based gravity tests (Brack *et al.*[23]) and is similarly widespread in fluid dynamics (Trefethen *et al.*,[24] Schmid and Henningson,[25] and Trefethen and Embree[26]). The non-orthogonality between eigenspaces requires more refined projection techniques to accurately map initial conditions to the SSM-based basepoints of the stable fibers containing them.

To this end, Roberts[27] formulated a nonlinear partial differential equation to compute nonlinear oblique projections along the stable fibers for center manifolds. As this equation is difficult to solve in practice, Roberts[28] also proposed a numerical approach based on a series expansion around equilibria to approximate these projections.

In the context of input–output systems, the projection direction is connected to the observability and controllability of states. Highly observable states strongly influence future outputs, while highly controllable states are those most easily excited by inputs. These properties are quantified by the observability and controllability Gramians. Holmes *et al.*[29] showed that POD modes align with the dominant eigenvectors of the controllability Gramian, meaning that a projection onto these modes retains the most controllable states. However, system dynamics are more influenced by the most observable states, since perturbations in their direction significantly alter future outputs. Finding a coordinate transformation so that the most controllable states coincide with the most observable ones (i.e., observability and controllability Gramians are equal and diagonal for a linear system) is the idea behind the balanced truncation, pioneered by Mullis and Roberts[30] and Moore[31] and balanced POD (Rowley[32]) for linear time-invariant systems.

Projection in the balanced coordinates corresponds to an oblique projection along the fibers, inherently accounting for non-normality (see Antoulas[33] and Gugercin *et al.*[34]). Various formulations for linear time-invariant systems exist (see Gugercin and Antoulas,[35] and Benner and Breiten[36] for a review), and balanced POD has been widely applied to wall-bounded shear flows (see Ilak and Rowley,[37,38] Ahuja and Rowley,[39] Bagheri *et al.*,[40] and Barbagallo *et al.*[41]). Extensions to nonlinear systems were proposed by Scherpen[42] and Scherpen and Van der Schaft,[43] introducing energy functions as nonlinear analogs of the Gramians. The resulting nonlinear oblique projections, however, involve costly and ill-conditioned transformations (see Gray and Scherpen[44]). Recent efforts to approximate these energy functions via Taylor series expansions have improved computational tractability (Fujimoto and Tsubakino[45] and Kramer *et al.*[46,47]). Otto *et al.*[48] demonstrated that balancing adjoint-based sensitivity information with the variance of states along trajectories, in the construction of a linear oblique projection, already yields an accurate representation of nonlinear shear-dominated fluid flows.

Exact reconstruction of stable fibers from experimental data is particularly challenging, as trajectories decay exponentially fast toward the slow manifold, leaving limited information about the fiber geometry. An inspection of examples of Szalai[13,14] shows that an accurate recovery of the stable foliation near an SSM requires data volumes, resolutions, and initial condition distributions that are unfeasible in experimental settings. For instance, Szalai[14] approximates the local stable foliation of a 1D SSM in a 2D system using 500 trajectories with uniformly distributed initial conditions across the phase space. Moreover, the computational burden increases steeply with system dimension: while SSM reduction involves a single d-dimensional manifold, fiber reconstruction targets a d-dimensional family of $(n-d)$-dimensional manifolds. In continuum systems, this becomes intractable as $n \to \infty$.

Otto *et al.*[49] proposed a method for constructing nonlinear oblique projections using an autoencoder neural network, wherein the encoder enforces a projection and the decoder defines the manifold. The projection direction is learned by minimizing the discrepancy between the time derivative of projected trajectories and the reduced dynamics on the manifold. This approach requires large datasets, e.g., 1000 training trajectories in one example.

In many cases, a linear approximation of stable fibers is sufficient for effective model reduction, when non-normality between slow and fast eigenspaces dominates over nonlinear effects.[41,48,50–53]

For nonlinear, but linearizable systems, this is discussed in detail by Haller and Kaszás.[54]

As a recent development, Bettini *et al.*[15] have identified the overall impact of the fast dynamics in the data, rather than identifying the fast subspace itself. Specifically, they construct an oblique projection along stable fibers by finding the linear mapping from the full observable space to the slow spectral subspace that minimizes the oscillations in the backbone curve (i.e., instantaneous amplitude-frequency curve) of a decaying trajectory observed under that projection. This approach is highly data-efficient, enabling the reconstruction of decaying trajectories and the prediction of forced response curves from a single decaying trajectory in experimental data. The method, however, is limited to underdamped oscillatory systems reducible to 2D SSMs, for which well-defined backbone curves exist. Finally, Kogelbauer and Karlin[55] and Buurmeijer *et al.*[56] recently proposed methods that approximate oblique projections by minimizing long-term prediction errors. However, these approaches generally yield projections that violate foliation invariance and hence do not align with the true fiber directions.

In this work, we develop a new approach to oblique projections for SSM-based model reduction by exploiting foliation invariance. Specifically, we identify the correct projection direction along stable fibers and use it to construct a consistent SSM parametrization. While our treatment encompasses both linear and nonlinear oblique projections, linear oblique projections often already provide accurate results and can be realistically constructed from experimental data (see Bettini *et al.*[15]). Importantly, we do not attempt to reconstruct the full fast foliation or explicitly identify the fast subspace, as both of these are typically high (or even infinite) dimensional in practically relevant model reduction problems. Our approach is applicable to both oscillatory and non-oscillatory systems, regardless of the dimension of the SSM. It only requires experimentally feasible amounts of data, thus overcoming key limitations of prior methods.

The structure of this paper is as follows. In Sec. II, we review the concept of SSMs and present a method to parametrize them from trajectory data via general oblique projections along nonlinear and linear approximations of stable fibers. Section III implements this approach to obtain data-driven SSM-based reduced-order models using linear oblique projections. Finally, Sec. IV demonstrates the application of this new data-driven method to both numerical simulations and experimental data.

II. SETUP

A. Spectral submanifolds

Consider an autonomous dynamical system of the form

$$\dot{\boldsymbol{x}} = \boldsymbol{f}(\boldsymbol{x}) = \boldsymbol{A}\boldsymbol{x} + \boldsymbol{f}_0(\boldsymbol{x}), \quad \boldsymbol{x} \in \mathbb{R}^n, \quad \boldsymbol{A} \in \mathbb{R}^{n\times n}, \quad \boldsymbol{f}_0 \in \mathcal{C}^r, \quad \boldsymbol{f}_0 = \mathcal{O}\left(|\boldsymbol{x}|^2\right), \tag{1}$$

for some integer $r \geq 1$. We assume that $\boldsymbol{A}$ is diagonalizable and $\boldsymbol{f}(\boldsymbol{0}) = \boldsymbol{0}$, so that the origin is a fixed point of the system. We further assume that this fixed point is hyperbolic. Trajectories $\{\boldsymbol{x}(t;\boldsymbol{x}_0)\}_{t\in\mathbb{R}}$ of this system evolve from initial conditions $\boldsymbol{x}_0$. The flow map $\boldsymbol{F}^t : \mathbb{R}^n \to \mathbb{R}^n$ is defined as the mapping taking $\boldsymbol{x}_0$ at $t_0 = 0$ to the final position $\boldsymbol{x}$ at time t, i.e.,

$$\boldsymbol{F}^t(\boldsymbol{x}_0) = \boldsymbol{x}(t;\boldsymbol{x}_0). \tag{2}$$

In the linear part of system (1), each eigenvalue λ_j of the matrix $\boldsymbol{A}$ determines a corresponding real *eigenspace* E_j. The definition of the eigenspace E_j depends on whether λ_j is real or complex. When λ_j is a real eigenvalue, E_j is the one-dimensional span of the corresponding real eigenvector. When λ_j is a complex eigenvalue, the eigenspace E_j is spanned by the real and imaginary parts of one of the associated complex-conjugate eigenvectors, yielding a real two-dimensional invariant subspace. A *spectral subspace* S is the direct sum of ℓ such eigenspaces, i.e.,

$$S = S_{j_1} \oplus S_{j_2} \oplus \cdots \oplus S_{j_\ell}, \quad 1 \leq \ell \leq n. \tag{3}$$

For simplicity, we assume the $\boldsymbol{x} = \boldsymbol{0}$ fixed point is asymptotically stable, i.e., $\mathrm{Re}(\lambda_j) < 0$ for all j. Among all spectral subspaces, the one corresponding to the slowest decaying modes is of particular interest. Such a slow subspace, denoted by E, is associated with a group of eigenvalues of $\boldsymbol{A}$ whose real parts are closest to zero. As a result, generic trajectories of the linearized system decay faster toward E than they decay inside E.

As shown in Haller and Ponsionen,[11] based on the results by Cabré *et al.*,[10] under suitable smoothness and nonresonance conditions, E admits a unique nonlinear continuation in the full nonlinear system (1). This continuation is an invariant manifold, known as the *primary spectral submanifold* (SSM), and is denoted by $\mathcal{W}(E)$. The manifold $\mathcal{W}(E)$ is a class $\mathcal{C}^r$ invariant manifold that is tangent to E at the origin and has the same dimension as E. Furthermore, $\mathcal{W}(E)$ is the smoothest among all invariant manifolds with the same dimension and tangency properties. Therefore, the dynamics on $\mathcal{W}(E)$ gives a mathematically rigorous and the smoothest possible model of the full dynamics of system (1) with which all nearby trajectories synchronize exponentially fast.

B. Stable foliation in linear and nonlinear systems

Consider the linear part of system (1), namely,

$$\dot{\boldsymbol{x}} = \boldsymbol{A}\boldsymbol{x}. \tag{4}$$

The set $\mathcal{F}_{\boldsymbol{p}} \in \mathcal{R}^n$ of initial conditions that synchronize at the fastest rate with an initial condition $\boldsymbol{p} \in E$ is an $(n-d)$-dimensional plane, parallel to the fast subspace F so that $\mathcal{F}_{\boldsymbol{p}} \cap E = \boldsymbol{p}$. The plane $\mathcal{F}_{\boldsymbol{p}}$ is often called the stable fiber with basepoint $\boldsymbol{p}$ [see Fig. 1(a)].

In the corresponding nonlinear system (1), if the nonresonance conditions

$$\lambda_\ell \neq \sum_{j=1}^{n} m_j \lambda_j, \quad \ell = 1,\ldots,n, \quad m_j \in \mathbb{N}, \quad \sum_{j=1}^{n} m_j \geq 2 \tag{5}$$

are satisfied, then the $\mathcal{C}^r$-linearization result of Sternberg[57] implies the smooth persistence of the stable fibers of the linearized system (4) in the full nonlinear system (1) in a neighborhood U of the origin (see Haller[6] for more detail). Specifically, the stable fibers $\mathcal{F}_{\boldsymbol{p}}$ are $(n-d)$-dimensional, $\mathcal{C}^r$ smooth surfaces containing the initial conditions that converge to the trajectory through their basepoint $\boldsymbol{p} \in \mathcal{W}(E)$ at the fastest rate. As in the linear system (4), the stable

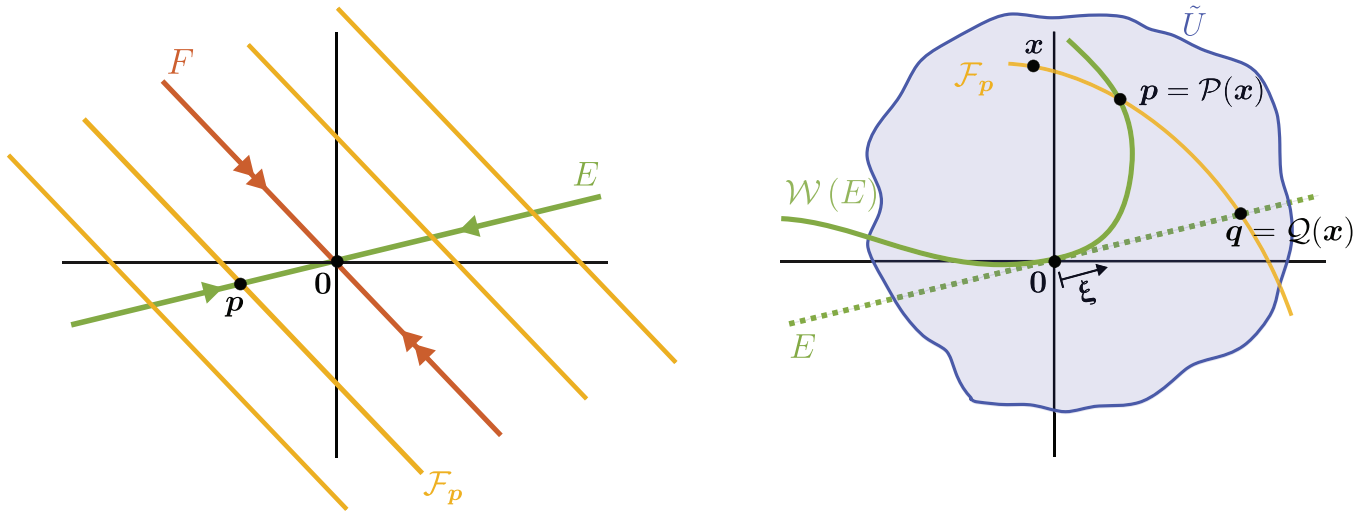

FIG. 1. Spectral submanifold and stable foliation geometry. (a) Linearized system (4). (b) Nonlinear system (1).

fibers of the nonlinear system (1) form an invariant family, i.e.,

$$\boldsymbol{F}^t\left(\mathcal{F}_{\boldsymbol{p}}\right) \subset \mathcal{F}_{\boldsymbol{F}^t(\boldsymbol{p})}, \quad t \geq 0. \tag{6}$$

In a neighborhood $\tilde{U} \subset U$ of the origin, the spectral subspace E is C^r-close to the SSM $\mathcal{W}(E)$ and hence each nonlinear stable fiber $\mathcal{F}_{\boldsymbol{p}}$ of system (1) intersects E transversely in a unique point $\boldsymbol{q} \in E$. As a consequence, if $\boldsymbol{V} \in \mathbb{R}^{n\times d}$ is a matrix whose columns form an orthonormal basis in E, then

$$\boldsymbol{\xi} = \boldsymbol{V}^{\mathrm{T}}\boldsymbol{q} \in \mathbb{R}^d \tag{7}$$

can be used as a coordinate representation of $\boldsymbol{q}$ within E. Furthermore, since $\boldsymbol{q}$ is in the range of $\boldsymbol{V}$, we have $\boldsymbol{q} = \boldsymbol{V}\boldsymbol{k}$ for some $\boldsymbol{k} \in \mathbb{R}^d$, and hence

$$\boldsymbol{V}\boldsymbol{\xi} = \boldsymbol{V}\boldsymbol{V}^{\mathrm{T}}\boldsymbol{q} = \boldsymbol{V}\boldsymbol{V}^{\mathrm{T}}\boldsymbol{V}\boldsymbol{k} = \boldsymbol{V}\boldsymbol{k} = \boldsymbol{q}, \tag{8}$$

where we have used $\boldsymbol{V}^{\mathrm{T}}\boldsymbol{V} = \boldsymbol{I} \in \mathbb{R}^{d\times d}$.

Let $\mathcal{P} : \mathcal{F}_{\boldsymbol{p}} \mapsto \boldsymbol{p}$ denote the projection map from the stable fiber $\mathcal{F}_{\boldsymbol{p}}$ to its basepoint, $\boldsymbol{p} \in \mathcal{W}(E)$. Similarly, let $\mathcal{Q} : \mathcal{F}_{\boldsymbol{p}} \cap \tilde{U} \mapsto E$ denote the map taking $\boldsymbol{x} \in \mathcal{F}_{\boldsymbol{p}}$ to the unique intersection point $\boldsymbol{q}$ of $\mathcal{F}_{\boldsymbol{p}}$ with E, i.e.,

$$\mathcal{Q} : \boldsymbol{x} \mapsto \boldsymbol{q} = \mathcal{F}_{\boldsymbol{p}} \cap E, \quad \boldsymbol{x} \in \mathcal{F}_{\boldsymbol{p}} \cap \tilde{U}. \tag{9}$$

We note the relations

$$\mathcal{P} \circ \mathcal{P} = \mathcal{P}, \quad \mathcal{Q} \circ \mathcal{Q} = \mathcal{Q}. \tag{10}$$

In terms of the $\boldsymbol{\xi}$ coordinates of $\boldsymbol{q}$, $\boldsymbol{V}^{\mathrm{T}}\mathcal{Q}$ induces a projected flow $\boldsymbol{S}^t : \mathbb{R}^d \to \mathbb{R}^d$ that can be used to track the time evolution of the fiber basepoint $\boldsymbol{p}$ in the $\boldsymbol{\xi}$ coordinates. Specifically, from the relations (8) and (9), we obtain

$$\boldsymbol{S}^t\left(\boldsymbol{V}^{\mathrm{T}}\mathcal{Q}(\boldsymbol{x})\right) = \boldsymbol{V}^{\mathrm{T}}\mathcal{Q}\left(\boldsymbol{F}^t(\boldsymbol{x})\right). \tag{11}$$

Fixing the initial condition $\boldsymbol{x}$, differentiating (11) with respect to t and setting $t = 0$ gives

$$\dot{\boldsymbol{\xi}} = \boldsymbol{r}(\boldsymbol{\xi}) = \boldsymbol{V}^{\mathrm{T}}\boldsymbol{D}\mathcal{Q}(\boldsymbol{x})\boldsymbol{f}(\boldsymbol{x}), \quad \boldsymbol{\xi} = \boldsymbol{V}^{\mathrm{T}}\mathcal{Q}(\boldsymbol{x}), \quad \boldsymbol{r}(\boldsymbol{\xi}) := \frac{\partial}{\partial t}\boldsymbol{S}^t(\boldsymbol{\xi})\Big|_{t=0}. \tag{12}$$

We also note that the mapping

$$\hat{\boldsymbol{h}} : E \cap \tilde{U} \to \mathcal{W}(E), \quad \hat{\boldsymbol{h}}(\boldsymbol{q}) = \boldsymbol{p}, \tag{13}$$

is a C^r diffeomorphism between the fiber points $\boldsymbol{p}$, $\boldsymbol{q} \in \mathcal{F}_{\boldsymbol{p}}$. By Eqs. (13) and (8), we also obtain another diffeomorphism

$$\boldsymbol{h} : \mathbb{R}^d \to \mathcal{W}(E), \quad \boldsymbol{h}(\boldsymbol{\xi}) = \hat{\boldsymbol{h}}\left(\boldsymbol{V}\boldsymbol{\xi}\right), \tag{14}$$

which gives $\mathcal{W}(E)$ as an embedding of $E \cap \tilde{U}$ into $\mathbb{R}^n$. Since $\mathcal{W}(E)$ is invariant, it satisfies the invariance equation

$$\dot{\boldsymbol{x}}|_{\mathcal{W}(E)} = \boldsymbol{D}\boldsymbol{h}|_{\mathcal{W}(E)}\dot{\boldsymbol{\xi}}. \tag{15}$$

1. Example 1

To illustrate the concepts introduced so far, let us consider the system

$$\begin{aligned} \dot{x}_1 &= -\alpha x_1 + \delta x_2 + \mu x_2^2 \\ \dot{x}_2 &= -\beta x_2 + \gamma x_1^2 \end{aligned}, \quad \beta > \alpha > 0. \tag{16}$$

Noting that the 1D slow spectral subspace is $E = \{\boldsymbol{x} \in \mathbb{R}^2 | x_2 = 0\}$, we seek the slow SSM $\mathcal{W}(E)$ in the form

$$\begin{aligned} x_1 &= h_1(\xi) = h_{11}\xi + h_{12}\xi^2 + \mathcal{O}(\xi^3), \\ x_2 &= h_2(\xi) = h_{21}\xi + h_{22}\xi^2 + \mathcal{O}(\xi^3), \end{aligned} \tag{17}$$

with the reduced dynamics

$$\dot{\xi} = r(\xi) = r_1\xi + r_2\xi^2 + \mathcal{O}(\xi^3). \tag{18}$$

Here the reduced coordinate ξ within E is defined by the still unknown nonlinear projection

$$\xi = \boldsymbol{V}^{\mathrm{T}}\mathcal{Q}(\boldsymbol{x}). \tag{19}$$

Given that the tangent space is $\boldsymbol{V} = (1, 0)^{\mathrm{T}}$, Eq. (19) can be written in the form (see Appendix A)

$$\xi = k_1x_1 + k_2x_2 + k_3x_1^2 + k_4x_1x_2 + k_5x_2^2 + \mathcal{O}(|\boldsymbol{x}|^3). \tag{20}$$

Imposing conditions (10) yields $k_1 = 1$ and $k_3 = 0$. Moreover, equating powers of x_1 and x_2 in the invariance equation (12), we obtain the stable fibers satisfying the equations

$$\begin{aligned} \xi = \boldsymbol{V}^{\mathrm{T}}\mathcal{Q}(\boldsymbol{x}) = x_1 &+ \frac{\delta}{\beta-\alpha}x_2 - \frac{2\gamma}{\beta}\left(\frac{\delta}{\beta-\alpha}\right)^2 x_1x_2 \\ &+ \frac{1}{2\beta-\alpha}\left\{\mu - \gamma\left(\frac{\delta}{\beta-\alpha}\right)^2\left[2\frac{\delta}{\beta} + \left(\frac{\delta}{\beta-\alpha}\right)\right]\right\}x_2^2 \\ &+ \mathcal{O}(|\boldsymbol{x}|^3) \end{aligned} \tag{21}$$

and the reduced dynamics

$$\dot{\xi} = r(\xi) = -\alpha\xi + \gamma\frac{\delta}{\beta-\alpha}\xi^2 + \mathcal{O}(\xi^3). \tag{22}$$

Finally, exploiting the fact that the tangent space is spanned by $\boldsymbol{V} = (1, 0)^{\mathrm{T}}$ and equating powers of ξ in the invariance equation for the SSM (15) gives

$$\begin{aligned} x_1 &= \xi - \frac{\gamma\delta}{(\beta-\alpha)(\beta-2\alpha)}\xi^2 + \mathcal{O}(\xi^3), \\ x_2 &= \frac{\gamma}{\beta-2\alpha}\xi^2 + \mathcal{O}(\xi^3). \end{aligned} \tag{23}$$

This example also illustrates the crucial role of the nonresonance condition (5) in guaranteeing the existence of the SSM, as potential resonant terms appear in the denominator of Eq. (23). Appendix A provides further details on how to ensure that all unknowns in the oblique projection, the reduced dynamics, and the SSM parametrization can be uniquely identified.

The phase space geometry and the computed quantities are shown in Fig. 2.

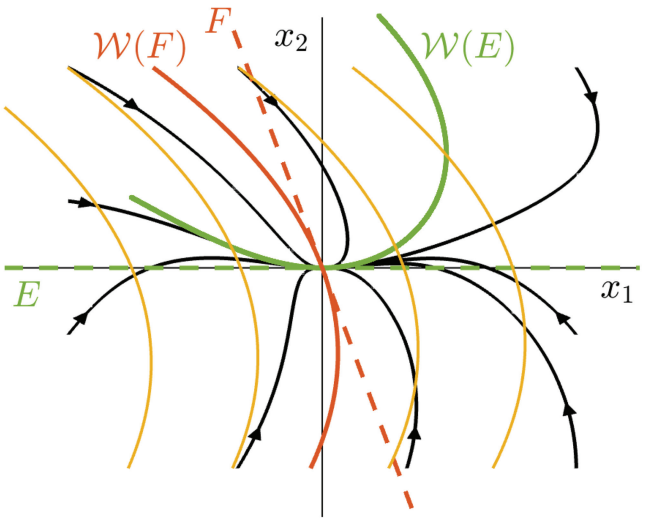

FIG. 2. Phase space of Example 1. The slow SSM, $\mathcal{W}(E)$, is parametrized as an embedding of E into $\mathbb{R}^2$ along the stable fibers according to Eq. (23). The SSM is plotted by substituting Eq. (21) into Eq. (23) and solving for a range of x_1 and x_2 values, while the fibers are plotted by implicitly solving Eq. (21) for various base points. Notably, the fiber passing through the origin corresponds to the fast SSM, $\mathcal{W}(F)$. The values of the parameters are $\alpha = 1$, $\beta = 2.7$, $\delta = 0.5$, $\mu = 1.5$, and $\gamma = 0.7$.

C. Linear oblique projections

In certain systems, the geometry of fibers is primarily shaped by the non-orthogonality of slow and fast eigenspaces, rather than by nonlinear effects. Furthermore, in many experimental applications, the data tend to lie close to the primary SSM, as trajectories converge to it rapidly. As the numerical and experimental examples in Bettini *et al.*[15] show in such situations a linear oblique projection is sufficient to approximate the stable fiber geometry near the slow SSM. In the ideal limit of exactly linear fibers, this projection would recover the fiber geometry exactly. Away from this limit, the linear oblique projection is a local approximation of the true nonlinear fiber geometry. Under such a linear approximation, we have a linear oblique projection

$$\boldsymbol{q} = \mathcal{Q}(\boldsymbol{x}) = \boldsymbol{Q}\boldsymbol{x}, \quad \boldsymbol{Q} \in \mathbb{R}^{n\times n}, \tag{24}$$

which induces the reduced coordinates

$$\boldsymbol{\xi} = \boldsymbol{V}^{\mathrm{T}}\boldsymbol{Q}\boldsymbol{x}. \tag{25}$$

The invariance equation (12) now reads

$$\boldsymbol{V}^{\mathrm{T}}\boldsymbol{Q}\boldsymbol{f}(\boldsymbol{x}) = \boldsymbol{r}\left(\boldsymbol{V}^{\mathrm{T}}\boldsymbol{Q}\boldsymbol{x}\right). \tag{26}$$

The condition

$$\boldsymbol{Q}\boldsymbol{V} = \boldsymbol{V} \tag{27}$$

ensures that the range of the projection $\boldsymbol{Q}$ coincides with the slow spectral subspace E, tangent to the primary slow SSM $\mathcal{W}(E)$. As shown in Banerjee and Roy,[58] any linear projection operator $\boldsymbol{Q}$ can be decomposed as

$$\boldsymbol{Q} = \boldsymbol{V}\left(\boldsymbol{B}^{\mathrm{T}}\boldsymbol{V}\right)^{-1}\boldsymbol{B}^{\mathrm{T}}, \tag{28}$$

where the columns of $\boldsymbol{B} \in \mathbb{R}^{n\times d}$ span $F^{\perp}$, the orthogonal complement of the fast subspace F and kernel of the projection $\boldsymbol{Q}$, as seen in Fig. 3. The decomposition (28) enforces the idempotency of the

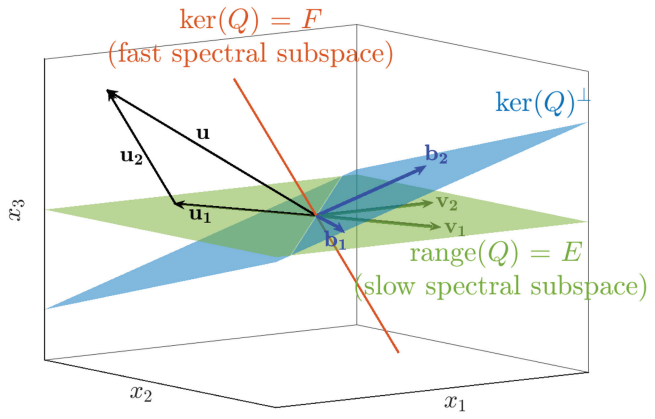

FIG. 3. Geometry of the linear oblique projection $\boldsymbol{Q}$. Figure adapted from Bettini *et al.*, Chaos **35**, 043135 (2025). Copyright 2025 Author(s), licensed under a Creative Commons Attribution (CC BY) license.[15]

projection $\boldsymbol{Q}$ by construction. Plugging the decomposition (28) into Eq. (26), subject to the constraint (27), we obtain

$$\boldsymbol{B}^{\mathrm{T}}\dot{\boldsymbol{x}} = \boldsymbol{B}^{\mathrm{T}}\boldsymbol{V}\boldsymbol{r}\left(\left(\boldsymbol{B}^{\mathrm{T}}\boldsymbol{V}\right)^{-1}\boldsymbol{B}^{\mathrm{T}}\boldsymbol{x}\right). \tag{29}$$

Equation (29) shows that enforcing the invariance of the foliation via linear oblique projection onto E is equivalent to imposing invariance via the orthogonal projection onto $F^{\perp}$, where F is the fast subspace and the kernel of the oblique projection. Furthermore, as noted by Rowley and Dawson[2] and Bettini *et al.*,[15] it is more practical to work with $F^{\perp}$ spanned by the columns of $\boldsymbol{B}$, rather than with F itself. This is because $F^{\perp}$ shares the same low dimensionality as the slow spectral subspace E, whereas F is typically high-dimensional. In fact, its dimension becomes infinite in practical applications involving continua.

III. DATA-DRIVEN MODELING OF STABLE FIBER PROPERTIES

Reconstructing the full slow foliation from data is impractical, as it requires capturing fast-decaying transients and hence demanding an extremely dense sampling of the phase space. This presents a fundamental challenge: on the one hand, accurate reduced-order modeling relies on the fast dynamics decaying quickly toward the primary SSM; on the other hand, reconstructing the foliation requires access to precisely those transient components that vanish quickly. As an inspection of previous equation-driven efforts for fiber reconstruction shows (Szalai[13,14] and Otto *et al.*[49]), resolving the foliation structure typically requires hundreds or even thousands of trajectories. In a purely data-driven setting, fiber reconstruction is often proceeded by *ad hoc* fits of very low dynamical systems to the data to keep the dimension of the fast subspace low (Szalai[14]).

As already noted, an exact nonlinear reconstruction of the stable foliation is often unnecessary and a linear approximation of the stable fibers near the underlying slow SSM suffices (see Fig. 4). Building on the observation that typical experimental initial conditions fall on fractional SSMs, Bettini *et al.*[15] developed a data-efficient method to approximate the projection along stable fibers linearly. This approach identifies the oblique projection that minimizes oscillations in the backbone curve and can approximate the local stable foliation near a slow SSM using a single decaying trajectory. A limitation of this approach is that it is only applicable to two-dimensional SSMs constructed over oscillatory linear modes.

Here, we overcome these limitations by computing the linear oblique projection by solving the foliation's invariance equation (29), as detailed below. This enables the simultaneous identification of the reduced coordinates parametrizing the SSM and its reduced dynamics. Related data-driven approaches also learn reduced coordinates together with reduced dynamics (see Champion *et al.*[59] and Padovan *et al.*[60]). In contrast to the autoencoder-SINDy approach of Champion *et al.*,[59] our method derives the reduced coordinates from the invariance of the fiber foliation rather than from representation learning. While Padovan *et al.*,[60] similarly to Otto *et al.*,[49] define reduced coordinates via oblique projections relative to the manifold, here obliqueness refers to the non-normal orientation between slow and fast subspaces. Moreover, those studies focus on numerical examples, whereas the present work also demonstrates applicability to experimental data.

The proposed procedure applies to observable data from an autonomous dynamical system and consists of the following steps:

1. **Identifying the SSM and observable space dimensions.** In the presence of oscillatory behavior, we perform a spectrogram analysis of the decaying data by examining its power spectral density (PSD), which reveals the number of active modes contained in the signal in time. The dimension d of the corresponding SSM is then given by the dimension of the real spectral subspace required to accommodate these active modes persisting in time. In contrast, for non-oscillatory (overdamped) decaying experimental data, we infer that the dynamics evolve on a dominant 1D SSM and, therefore, $d = 1$. By Whitney's embedding theorem,[61] such a d-dimensional SSM can generically be embedded in a p-dimensional observable space as long as $p > 2d$. Similarly, the Takens delay embedding theorem[22] guarantees under nondegeneracy conditions that the d-dimensional SSM can be embedded in a space formed by p delayed observations of a single generic observable $s(t)$ as long as $p > 2d$. In practice, larger values of delay-embedding space dimension p are often required, since the data do not lie exactly on the SSM to be embedded. Specifically, the delay-embedded vector $\boldsymbol{x} \in \mathbb{R}^p$ is formed as
$$\boldsymbol{x} = \left[s(t), s(t+\tau), s(t+2\tau), \ldots, s\left(t+(p-1)\tau\right)\right]^{\mathrm{T}}, \tag{30}$$
where τ is the time delay.
2. **Tangent space computation.** The tangent space E to the primary SSM contains the reduced coordinates used to parametrize the manifold. We seek a matrix $\boldsymbol{V} \in \mathbb{R}^{p\times d}$ whose columns span E. Moreover, we enforce the additional constraint $\boldsymbol{V}^{\mathrm{T}}\boldsymbol{V} = \mathbf{I}$, such that $\boldsymbol{V}^{\mathrm{T}}\boldsymbol{Q}\boldsymbol{V} = \boldsymbol{V}^{\mathrm{T}}\boldsymbol{V} = \mathbf{I}$. In practice, $\boldsymbol{V}$ is typically computed using singular value decomposition (SVD) on decaying data (see Bettini *et al.*[15] and Axås *et al.*[18]).
3. **Oblique projection and reduced dynamics computation.** We now aim to determine a linear oblique projection that

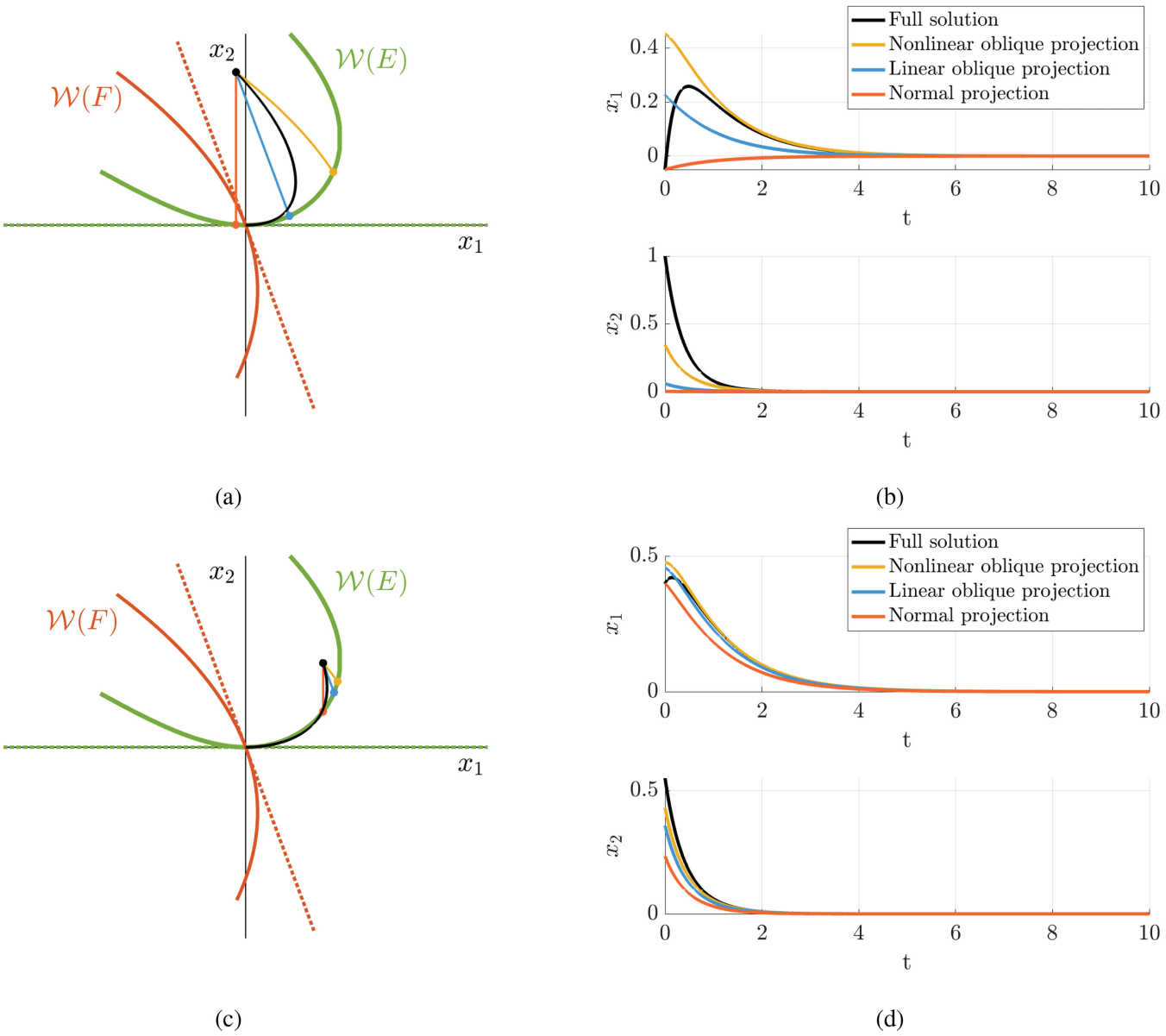

FIG. 4. Comparison of different projection methods onto the slow SSM $\mathcal{W}(E)$ to determine the reduced initial condition from a given initial condition in the phase space. Top: initial condition far from $\mathcal{W}(E)$. Bottom: initial condition near $\mathcal{W}(E)$.

approximates the exact fiber properties $\boldsymbol{Q}$ introduced in Eq. (28). Specifically, we seek the matrix $\boldsymbol{B} \in \mathbb{R}^{p\times d}$, while simultaneously identifying the coefficients of the reduced dynamics. We approximate the reduced dynamics as a multivariate polynomial of degree r

$$\dot{\boldsymbol{\xi}} = \boldsymbol{R}_{1:r}\boldsymbol{\xi}^{1:r}, \quad \boldsymbol{R}_{1:r} \in \mathbb{R}^{d\times r_i}, \tag{31}$$

where $\boldsymbol{\xi}^{1:r}$ denotes the vector of all monomials up to degree r in the reduced coordinates. To compute both $\boldsymbol{B}$ and $\boldsymbol{R}_{1:r}$, we solve the following optimization problem:

$$\left(\boldsymbol{B}^{\star}, \boldsymbol{R}^{\star}_{1:r}\right) = \arg\min_{\boldsymbol{B},\boldsymbol{R}_{1:r}} \left\| \boldsymbol{B}^{\mathrm{T}}\dot{\boldsymbol{x}} - \boldsymbol{B}^{\mathrm{T}}\boldsymbol{V}\boldsymbol{R}_{1:r}\left(\left(\boldsymbol{B}^{\mathrm{T}}\boldsymbol{V}\right)^{-1}\boldsymbol{B}^{\mathrm{T}}\boldsymbol{x}\right)^{1:r}\right\|^2, \tag{32}$$

where $\|\cdot\|$ refers to the 2-norm. The initial guesses for $\boldsymbol{B}$ and $\mathbf{R_{1:r}}$ are constructed, respectively, from $\boldsymbol{V}$ and a diagonal matrix

of eigenvalues corresponding to the slow subspace of the linearized dynamics, with the nonlinear terms initially set to zero. The optimization problem is solved through the BFGS Quasi-Newton algorithm (see Broyden,[62] Fletcher,[63] Goldfarb,[64] and Shanno[65]) for unconstrained multivariable optimization problems. Equation (32) involves the numerical time derivative of the data, which we compute using finite differences. The accuracy of this approximation is crucial for overall model quality. For this reason, we employ a central finite-difference scheme based on four adjacent points in each time direction.[66] To ensure stability of the numerical differentiation, noisy data are preliminarily bandpass filtered, retaining the persistent frequencies identified in the spectrogram while removing components due to experimental acquisition and measurement noise.The resulting oblique projection is

$$\boldsymbol{Q}^{\star}=\boldsymbol{V}\left(\boldsymbol{B}^{\star\mathrm{T}}\boldsymbol{V}\right)^{-1}\boldsymbol{B}^{\star\mathrm{T}}. \tag{33}$$

The reduced coordinates used to parametrize the SSM and describe the reduced dynamics are then obtained as

$$\boldsymbol{\xi}=\boldsymbol{V}^{\mathrm{T}}\boldsymbol{Q}^{\star}\boldsymbol{x}. \tag{34}$$

4. **SSM parametrization computation.** We approximate the primary SSM, $\mathcal{W}(E)$, as an embedding of its tangent space E, using a multivariate polynomial of order m. The manifold is expressed as

$$\boldsymbol{x}=\boldsymbol{V}\boldsymbol{\xi}+\boldsymbol{M}_{2:m}\boldsymbol{\xi}^{2:m}, \tag{35}$$

where $\boldsymbol{\xi}^{2:m}$ denotes the collection of all monomials in $\boldsymbol{\xi}$ of degree 2 to m and $\boldsymbol{M}_{2:m}$ contains the corresponding coefficients. These coefficients are determined by solving the following constrained regression problem:

$$\boldsymbol{M}^{\star}_{2:m}=\arg\min_{\boldsymbol{M}_{2:m}}\left\|\boldsymbol{x}-\boldsymbol{V}\boldsymbol{\xi}-\boldsymbol{M}_{2:m}\boldsymbol{\xi}^{2:m}\right\|^{2}, \tag{36}$$

subject to the constraint

$$\boldsymbol{V}^{\mathrm{T}}\boldsymbol{Q}\boldsymbol{M}_{2:m}=\boldsymbol{0}. \tag{37}$$

IV. APPLICATIONS

To illustrate the algorithm described in Sec. III, we begin with a 2D system with real modes, then consider a system with mixed oscillatory and real modes, previously studied by Otto *et al.*[49] For this system, we show that the algorithm developed here achieves accurate data-driven model reduction using orders of magnitude fewer trajectories. Next, we apply our approach to a 4D system, followed by several experimental case studies comparing orthogonal and oblique projection methods.

In these examples, we use the normalized mean trajectory error (NMTE) as a measure of the average deviation between the predicted and actual trajectories to assess the accuracy of the data-driven model we obtain. As introduced by Cenedese *et al.*,[16] the NMTE is defined as

$$\mathrm{NMTE}=\frac{\frac{1}{N}\sum_{j=1}^{N}\left\|\boldsymbol{x}(t_j)-\hat{\boldsymbol{x}}(t_j)\right\|}{\max_{1\le j\le N}\left\|\boldsymbol{x}(t_j)\right\|}, \tag{38}$$

where $\boldsymbol{x}$ denotes the true trajectory, $\hat{\boldsymbol{x}}$ denotes the corresponding model prediction, and N denotes the total number of observations.

A. Two-dimensional problem with real modes

We first reconsider the *Example 1* [see Eq. (16)] with parameters $\alpha=1$, $\beta=2.7$, $\delta=0.8$, $\mu=0.2$, and $\gamma=0.15$. As seen in Fig. 5(a), the nonlinear stable fibers in this problem are well approximated by a linear foliation, over the 1D slow SSM. In this example, the full phase space is assumed to be observable. Three trajectories are used for training, and both the SSM and its reduced dynamics are approximated through quadratic polynomials. The method is then tested on a trajectory located far from the primary SSM [black thick line in Fig. 5(a)]. As seen in Figs. 5(a) and 5(b), the oblique projection yields the optimal initial condition on the SSM, whose time evolution converges to the true trajectory the fastest, achieving NMTE = 1%. In contrast, the SSM-based model constructed with orthogonal projection onto the SSM produces NMTE = 2.2%.

B. Vortex shedding behind a cylinder

We now consider the system studied in Otto *et al.*,[49] originally introduced by Noack *et al.*[67] as a simplified model for vortex shedding behind a circular cylinder,

$$\begin{aligned}\dot{x}_1&=\alpha x_1-\omega x_2+\gamma x_1x_3,\\ \dot{x}_2&=\omega x_1+\alpha x_2+\gamma x_2x_3,\\ \dot{x}_3&=-\beta\left(x_3-x_1^2-x_2^2\right),\end{aligned} \tag{39}$$

with parameters $\alpha=0.1$, $\omega=1$, $\gamma=-0.1$, and $\beta=10$. This system features a saddle-type fixed point at the origin and an attracting limit cycle on the 2D unstable manifold of the fixed point.

In our setting, orthogonality or obliqueness is defined with respect to the tangent space E of the SSM at the origin. In contrast, Otto *et al.*[49] define these projection types with respect to the manifold itself. In this example, what is termed oblique projection in their work corresponds to an orthogonal projection in our formulation, since the foliation in this example turns out to be orthogonal to the tangent space E, as can be verified from Eq. (39).

As a further difference, while the approach of Otto *et al.*[49] requires training on 1000 trajectories to reconstruct the SSM and fiber directions via an autoencoder, the method developed here achieves the same using only two trajectories.

Figure 5(c) shows the data-driven fifth-order approximation of the 2D SSM parametrization and a linear approximation of the fibers. As shown in Fig. 5(d), the reduced-order model accurately predicts the evolution of a test trajectory initialized far from the SSM, with an error of NMTE = 0.6%.

C. Mechanical oscillator chain

We now revisit the two benchmark examples from Bettini *et al.*[15] to enable direct comparison and show that the new

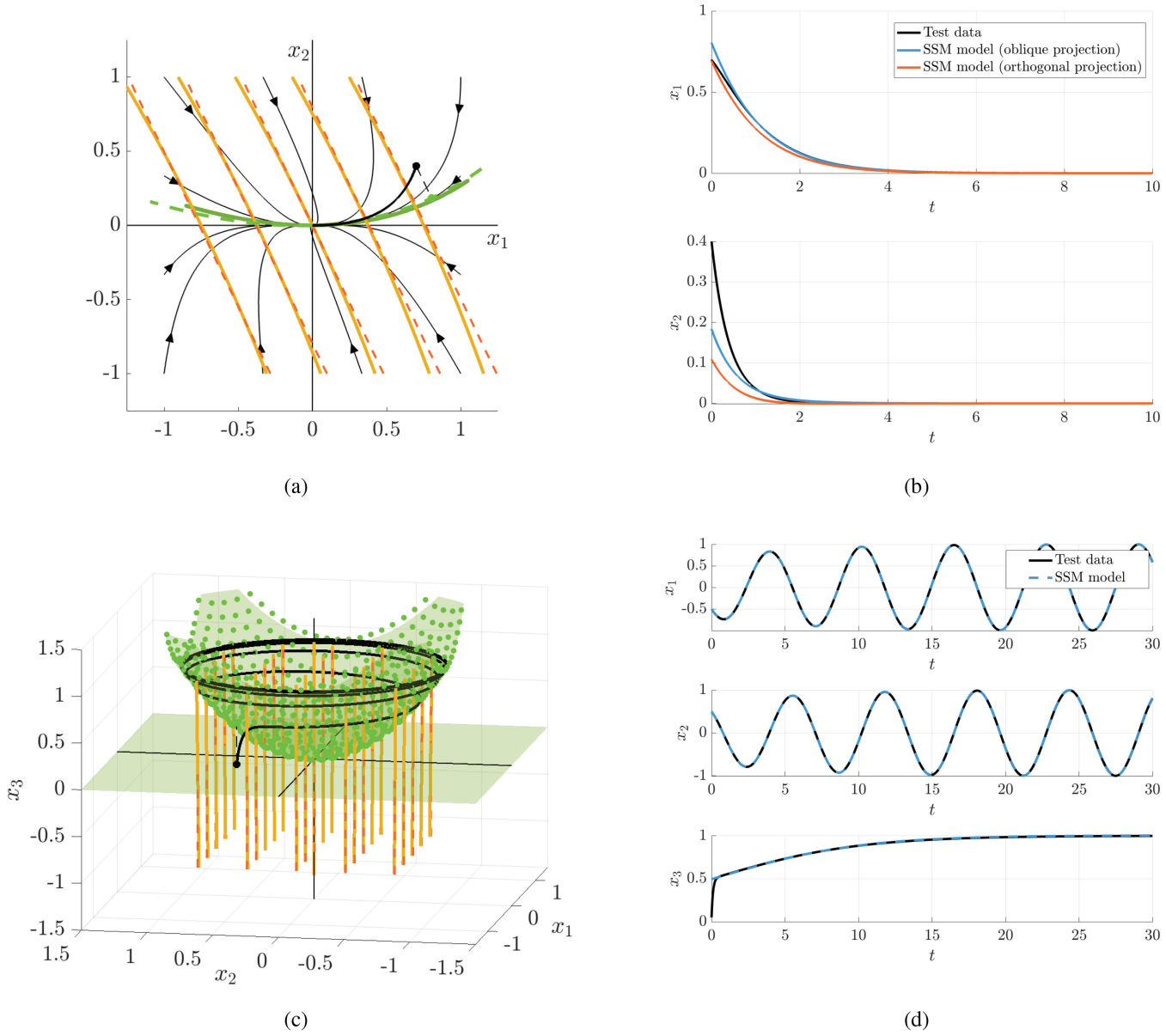

FIG. 5. Phase space representations of a two-dimensional system with real modes (a) and a 3D system with one oscillatory and one real mode (c). The green dashed line in (a) and green points in (c) represent the reconstructed SSMs obtained from data via the SSM-based model with linear oblique projection. The orange dashed lines show the reconstructed slow stable foliations, and the thick black lines denote the test trajectories. The plots (b) and (d) show the temporal comparison between the test trajectories and the model predictions, 1D in (b) and 2D in (d). In (b), both orthogonal and oblique projections are compared, whereas in (d), the two projections coincide.

method presented here achieves similar accuracy in predicting forced responses using only decaying trajectory data. These examples include numerical simulations of a two-degree-of-freedom mechanical system (see Fig. 6) and experimental data from a nonlinear beam, as discussed in Sec. IVA–C of Bettini *et al.*[15] The first system has two oscillatory modes ($n=4$), while the second is infinite-dimensional ($n=\infty$). In both cases, we seek a 2D, data-driven SSM-based reduced-order model ($d=2$), using a linear oblique projection to approximate the nonlinear fiber projection $\boldsymbol{Q}$.

Shown in Fig. 6, the mechanical system, slightly modified from that of Shaw and Pierre,[7] is observed through the coordinates $y_1=q_1$ and $y_2=q_2-q_1$, resulting in strongly non-normal slow and fast

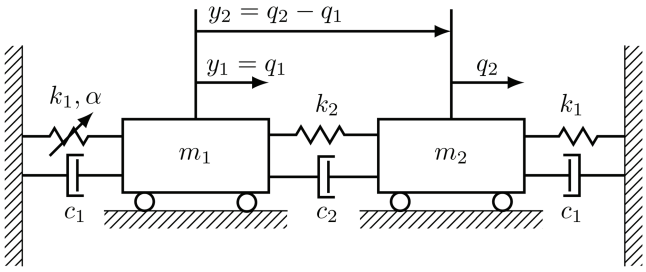

FIG. 6. Geometry of the two-degree-of-freedom mechanical system studied in Shaw and Pierre,[7] modified here by adding a damper between the left mass and the wall. Reproduced from Bettini *et al.*, Chaos **35**, 043135 (2025). Copyright 2025 Author(s), licensed under a Creative Commons Attribution (CC BY) license.

subspaces in phase space (see Bettini *et al.*[15]). This leads to oscillations in the backbone curve of decaying trajectories lying outside the primary SSM $\mathcal{W}(E)$, even in the linear regime [see Figs. 7(a) and 7(b), gray line]. The backbone is extracted from decaying data using the peak-finding and fitting (PFF) algorithm of Jin *et al.*[68] While Bettini *et al.*[15] exploited this linear-regime behavior to construct linear oblique projections, the present approach does not rely on identifying the linear regime or the availability of a backbone curve.

We perform an SSM reduction via oblique projection on the 2D slow manifold $\mathcal{W}(E)$ following the procedure in Sec. III. Using the notation therein, the phase space has dimension $n = 4$, the reduced model dimension is $d = 2$, and the observable space is the phase space ($p = n = 4$). Both the reduced dynamics and the SSM parametrization are approximated by polynomials up to order $r = m = 5$.

The SSM-reduced model is trained on a single decaying trajectory. As shown by Cenedese *et al.*[16] and implemented in the open-source code *SSMLearn*, backbone and forced response curve predictions can be extracted directly from the polar normal form of the SSM-reduced dynamics, without requiring numerical integration. As seen in Figs. 7(a) and 7(b), the results obtained using the method presented here are comparable to those reported in Bettini *et al.*,[15] but are obtained under less restrictive assumptions.

D. Experimental beam vibrations

Our next example from Bettini *et al.*[15] involves data from a nonlinear beam, experiment conducted by Brack *et al.*[23] A driven beam (transmitter) generates gravitational forces that excite a nearby resonator beam (receiver) through bending vibrations. The interaction between the transmitter and receiver beams is exploited to estimate the gravitational constant between the two beams. The forced response curves measured near the lowest bending modes of the transmitter beam exhibit pronounced nonlinear behavior [black dots in Figs. 7(c) and 7(d)].

We measure the velocity of the beam near one of its free ends. The spectrogram analysis of the decaying data suggests the presence of a single persisting mode, hence we choose $d = 2$. From this single scalar observable, we construct a $p = 6$ delay-embedded state vector

$$\boldsymbol{\eta} = \big(v(t), v(t+\Delta t), \ldots, v(t+(p-1)\Delta t)\big)^{\mathrm{T}}, \tag{40}$$

where $v(t)$ denotes the single velocity measurement at the laser measurement point and $\Delta t = 6 \times 10^{-4}$ s corresponds to the reciprocal of the sampling frequency. The choice of p satisfies the condition $p > 2d$, which ensures a valid embedding of the two-dimensional SSM via a generic observable (Takens[22]). The overembedding, i.e., value of p larger than the minimal needed to embed the manifold, helps the SSM identification, as the data do not lie exactly on it.

The training data consist of a single decaying trajectory, recorded after external forcing, applied at a specific amplitude and frequency, is switched off. Testing data consist of forced response curves collected at various excitation levels over a range of frequencies. Both the parametrization of the primary SSM $\mathcal{W}(E)$ and its reduced dynamics are approximated using seventh-order polynomials. As shown in Figs. 7(c) and 7(d), the method proposed here for constructing the linear oblique projection accurately reproduces the experimental forced response curves, yielding results comparable to those obtained by the approach presented in Bettini *et al.*[15]

In our data-driven identification of the oblique projection, as described in Sec. III, we solve the optimization problem (32). In this example, the initial condition for the matrix $\boldsymbol{B}$, which spans the orthogonal complement of the fast subspace, is obtained from the slowest mode of the adjoint of the linearized system.

E. Artificial muscle actuator for soft robotics

We now consider a second experimental example: an electrofluidic actuator known as a Hydraulically Amplified Self-Healing Electrostatic (HASEL) actuator, which serves as an artificial soft muscle in musculoskeletal robots (Acome *et al.*,[69] Buchner *et al.*,[70] Gravert *et al.*[71]). These actuators represent a particularly promising technology due to their simplicity, compliance, and high power density. Each HASEL unit consists of a polymer pouch filled with dielectric fluid and partially coated with compliant electrodes. Upon the application of high voltage, electrostatic forces induce deformation in the pouch, redistributing the internal fluid and generating a net contraction. Extension occurs passively in response to external forces, such as gravity, when a mass is attached at the actuator tip, or through antagonistic action in multi-actuator assemblies.

The experimental setup used in our study, shown in Fig. 8(b), was designed and fabricated by the Soft Robotics Lab at ETH (see Bettini *et al.*[72]) and consist of an array of 15 HASEL pouches. Each pouch is 4.5 cm wide and 2 cm long, with electrodes covering 50% of its surface. The shell is made from a 15 μm-thick heat-sealable Mylar film, while black carbon ink serves as the electrode material. Silicone oil is used as the dielectric fluid. Displacement measurements are obtained using a laser sensor positioned at the bottom of the actuator array.

Due to the complex coupling of soft material mechanics, electrostatics, fluid dynamics, and frictional contacts, developing a first-principles analytical model of HASEL actuators is extremely challenging. This motivates the use of data-driven modeling approaches, which are crucial for real-time control and integration of HASELs in more sophisticated artificial muscle systems (Bettini *et al.*[72]).

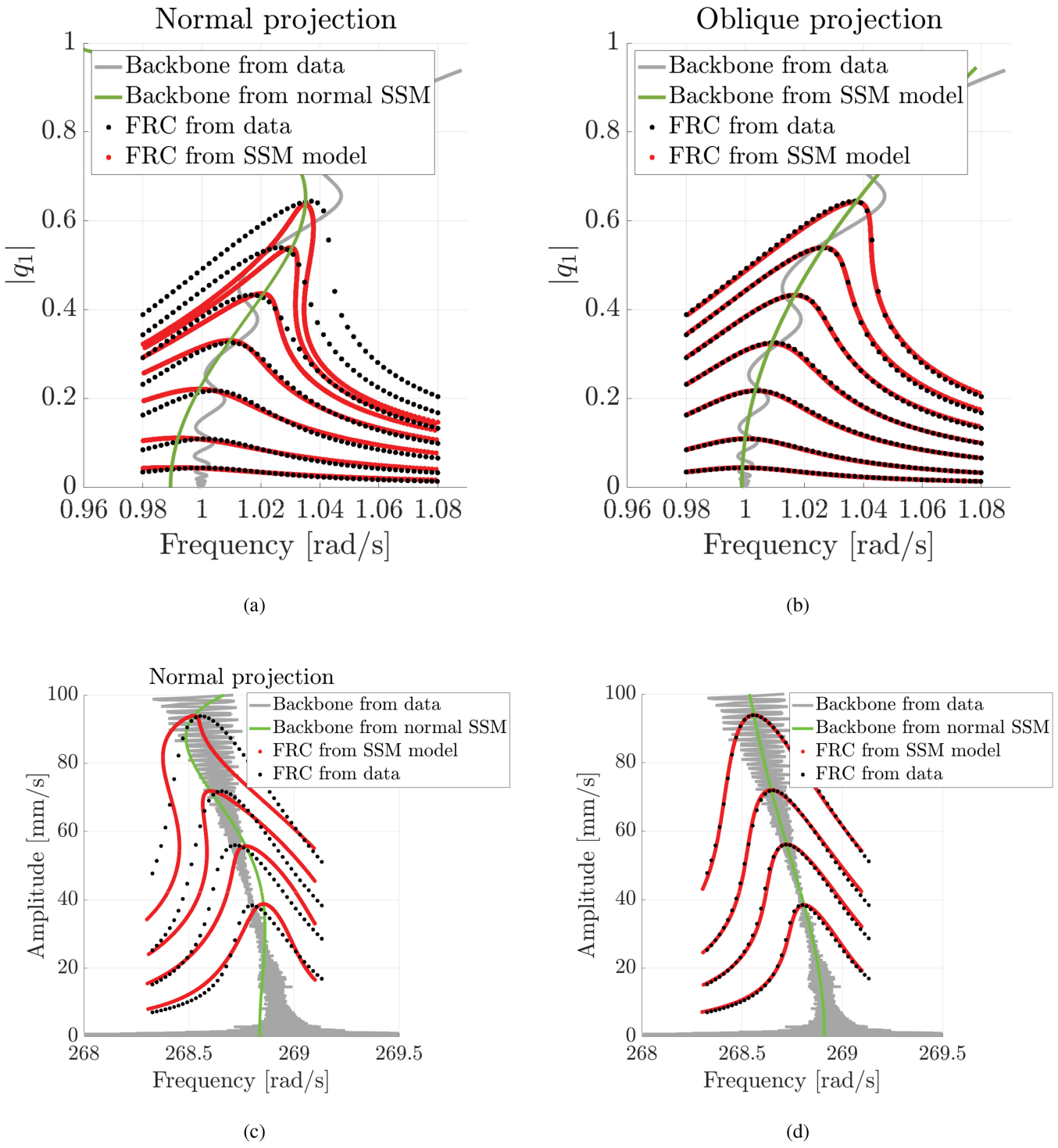

FIG. 7. Comparison of the predictions obtained from SSM-based reduced-order models using normal and oblique projections for the four-dimensional mechanical system [(a) and (b)] and the experimental nonlinear beam [(c) and (d)].

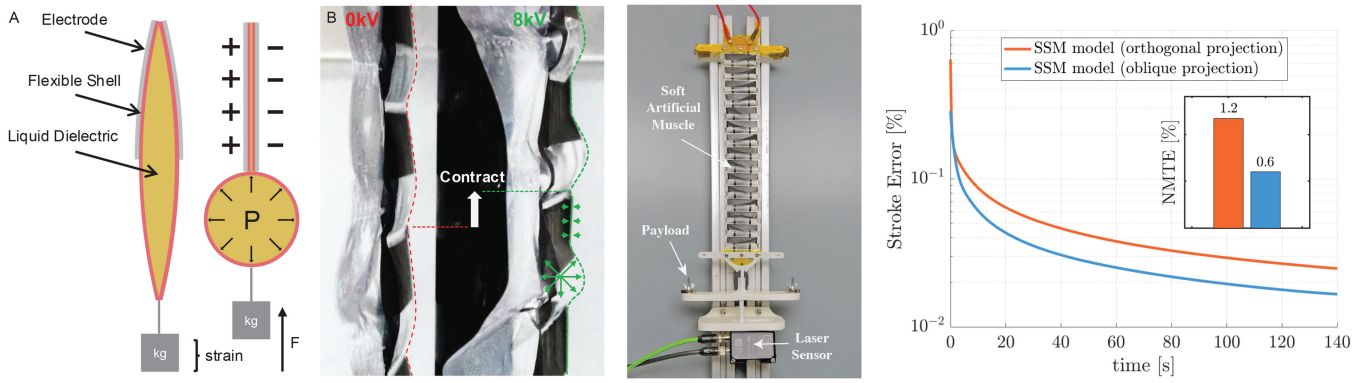

FIG. 8. HASEL actuator characterization and modeling. (a) Working principle of a HASEL actuator: electrostatic forces induced by high voltage application cause the polymer pouch to deform, redistributing the internal dielectric fluid and generating net contraction. (b) Experimental setup consisting of a Peano-HASEL with 15 pouches mounted vertically, with a payload and a laser sensor for the measurement system. (c) Comparison of prediction errors for a test trajectory using one-dimensional SSM-based reduced-order models constructed with orthogonal projection (magenta) and oblique projection (cyan).

Although adiabatic SSMs (Haller and Kaundinya[20]) are desirable for control purposes, the present work focuses instead on identifying the SSM of the autonomous system at a single operating condition, namely, under a constant applied voltage. Specifically, we fix the voltage at 6.5 kV and generate different initial conditions by applying sudden voltage perturbations around this reference value, followed by an immediate return to it. The system, though infinite-dimensional, exhibits underdamped decay in its laser-measured displacement response, indicating a dominant 1D SSM.

Figure 8(c) compares predictions of a test trajectory from one-dimensional SSM-based reduced-order models constructed using orthogonal and oblique projection in terms of the cumulative root mean square error (CRMSE), defined as

$$\mathrm{CRMSE}(t_k) = \frac{\sqrt{\frac{1}{k}\sum_{i=1}^{k}\left(x(t_i) - \hat{x}(t_i)\right)^2}}{\max|x|}, \tag{41}$$

where x and $\hat{x}$ denote the test trajectory and the corresponding model prediction. The two models achieve NMTEs of 1.2% and 0.4%, respectively.

Both the parametrization and reduced dynamics are approximated with fifth-order polynomials. The models are trained on a single decaying trajectory using a delay-embedded observable space with embedding dimension $p = 3$, constructed from delayed measurements of the scalar displacement observable. The training trajectory is taken among the dataset publicly available in Bettini *et al.*[72] Notably, the linear oblique projection employed here could not have been computed using the approach of Bettini *et al.*,[15] as the decaying trajectories under consideration exhibit no oscillatory behavior and therefore do not admit a well-defined backbone curve. In other words, the dominant dynamics is governed by a 1D slow SSM which is not accessible to the approach developed by Bettini *et al.*[15]

F. Resonant double beam

In our final example, we test our procedure using oblique projection-based SSMs of dimension greater than two. The experimental setup is the same as studied in Cenedese *et al.*,[17] consisting of a C-shaped external beam surrounding an internal beam, with the two beams connected through three bolts [see Fig. 9(a)]. Both beams are made of aluminum 6061-T6. Additionally, a linear spring connects the tip of the external beam to a fixed rigid frame in the transversal direction. Scalar transient velocity measurements of the inner beam tip, obtained via laser scanning vibrometry, reveal the presence of two resonant frequencies at 122.4 and 243.4 Hz, as shown in the spectrogram of Fig. 9(b). This indicates a 1:2 internal resonance, prompting the use of a 4D SSM-based reduced-order model to capture the two resonant modes. This is further confirmed by examining the data in reduced coordinates in Fig. 9(c), which cannot lie on a 2D SSM and instead require a higher-dimensional manifold reduction. Transient vibrations are recorded over 3 s at a sampling rate of 5120 Hz, generated by an impulse hammer applied at three different locations along the system span.

Using the same training data as in Cenedese *et al.*,[17] we observe that while the SSM-based reduction with orthogonal projection required a high-dimensional observable space ($p = 94$), the present approach with oblique projection allows a significant reduction in the observable space dimension to $p = 14$. This reduces the computational burden while yielding comparable results. The SSM parametrization and the reduced dynamics are approximated with a cubic order expansion, leading to the following reduced-order model in normal form coordinates

$$\begin{aligned}
\dot{\rho}_1 &= -0.46\rho_1 - 12.33\rho_1^3 + 0.20\rho_1\rho_2^2,\\
\dot{\theta}_1 &= 768.89 - 49.50\rho_1^2 - 4.55\rho_2^2,\\
\dot{\rho}_2 &= -3.12\rho_2 - 31.33\rho_1^2\rho_2 - 12.08\rho_2^4,\\
\dot{\theta}_2 &= 1529.31 - 41.19\rho_1^2 - 26.79\rho_2^2.
\end{aligned} \tag{42}$$

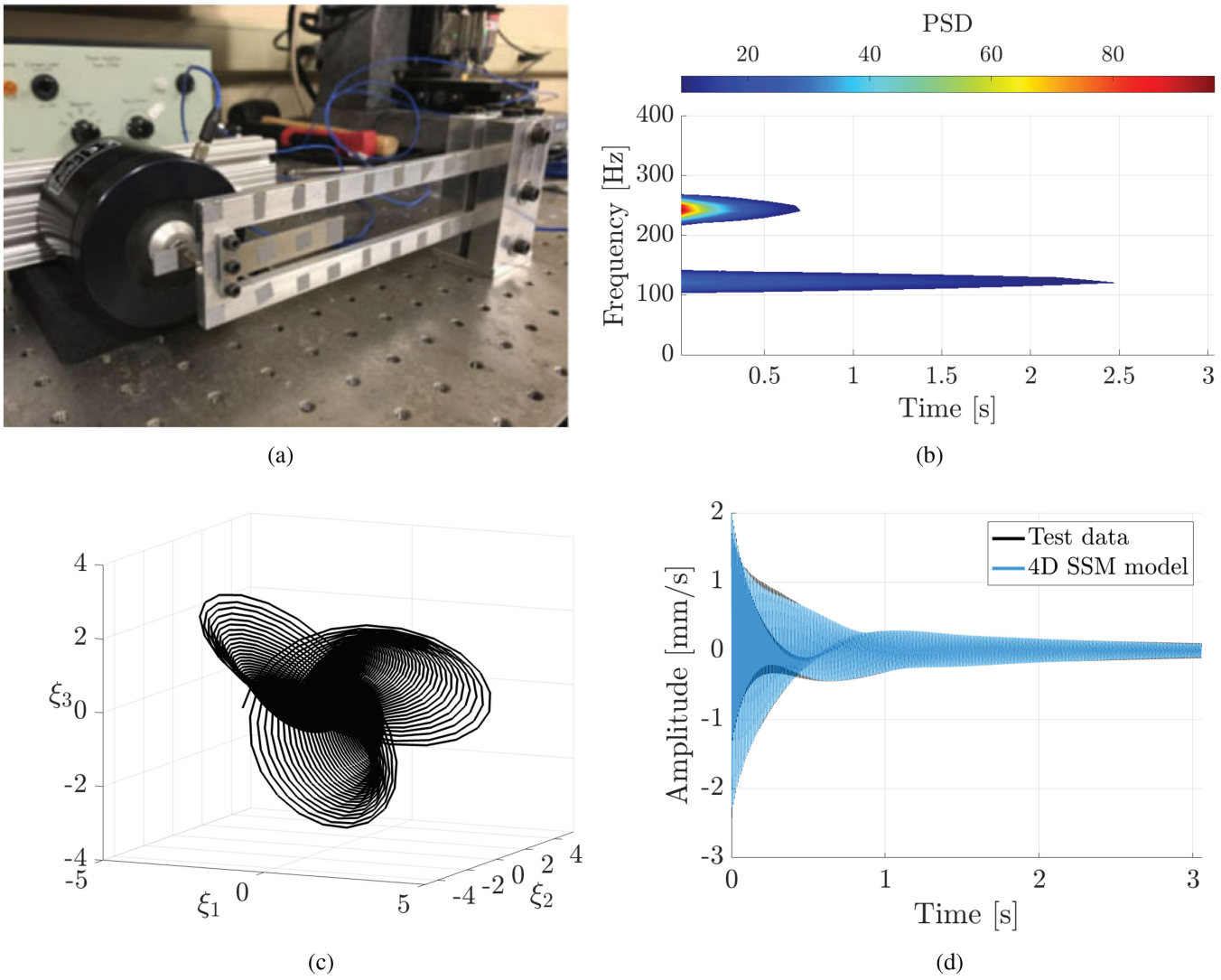

FIG. 9. (a) Experimental setup of the double beam system exhibiting a 1:2 internal resonance. (b) Spectrogram of the decaying data in terms of power spectral density (PSD), highlighting the two slow resonant modes. (c) Example of a training trajectory represented in three reduced coordinates. The underlying geometry of the data suggests that a reduction to a 2D SSM is insufficient, necessitating a higher-dimensional reduction. (d) Prediction of a test trajectory using the SSM-based reduced-order model constructed via oblique projection.

The SSM-reduced model (42) is then validated on test trajectories. Figure 9(d) shows the prediction of one test trajectory using the SSM-based reduced-order model with oblique projection, achieving an NMTE = 1.74%, compared to the NMTE = 1.95% using the SSM-based reduction with orthogonal projection used by Cenedese *et al.*[17]

V. CONCLUSIONS

We have extended data-driven SSM reduction to incorporate general oblique projections, independent of the dimension of the SSM and of the oscillatory or non-oscillatory nature of the modes contained in the underlying spectral subspace. This improves the *SSMLearn* algorithm for constructing SSM-based reduced-order models from data. Specifically, originally restricted to orthogonal projections onto slow subspaces and later extended to linear oblique projections for 2D oscillatory SSMs, the algorithm now accommodates linear oblique projections without constraints on the dimension of the SSM or the nature of the data, whether oscillatory or non-oscillatory.

Our methodology provides a well-founded procedure for constructing oblique projections from the full phase space, or, generally, from the space of observables, onto the slow subspace, along the directions defined by the stable fibers emanating from the SSM.

Importantly, we do not seek to reconstruct the full fast foliation or explicitly characterize the fast subspace, as these are prohibitively high (or even infinite) dimensional in practical model reduction problems.

In typical experimental settings, trajectories originate near the primary SSM and rapidly converge onto it. As these trajectories do not lie strictly on the SSM, they retain sufficient fast-mode content for a linear approximation of the oblique projection. Simultaneously, their rapid convergence ensures accurate recovery of both the SSM parametrization and the associated reduced dynamics. This observation allows our method to operate effectively with substantially less data than existing approaches, which generally require dense trajectory ensembles to resolve the full foliation structure.

We have applied this technique to various examples, both numerical and experimental, and across different SSM dimensions. While our current applications exhibit fast convergence to the primary SSM, thereby justifying the use of a linear approximation for the oblique projection, there may well exist systems in which this assumption fails. In such cases, a more accurate, nonlinear reconstruction of the fiber geometry from data may be necessary to further improve the fidelity of the SSM-based reduced-order model.

AUTHOR DECLARATIONS

Conflict of Interest

The authors have no conflicts to disclose.

Author Contributions

Leonardo Bettini: Conceptualization (lead); Data curation (lead); Formal analysis (lead); Investigation (lead); Methodology (lead); Software (lead); Validation (lead); Visualization (lead); Writing – original draft (lead); Writing – review & editing (lead). **Amirhossein Kazemipour:** Data curation (supporting); Visualization (supporting). **Robert K. Katzschmann:** Visualization (supporting); Writing – review & editing (supporting). **George Haller:** Conceptualization (lead); Methodology (equal); Project administration (lead); Supervision (lead); Writing – review & editing (lead).

DATA AVAILABILITY

The data that support the findings of this study are available in GitHub at https://github.com/haller-group/SSMLearn, Ref. 74.

APPENDIX A: REDUCTION ALONG NONLINEAR OBLIQUE PROJECTIONS IN EXAMPLE 1

In Example 1, we consider $\boldsymbol{x} = (x_1, x_2)^{\mathrm{T}} \in \mathbb{R}^n$ with $n = 2$, and we aim to construct a reduced-order model on the slow SSM, parametrized by $\xi \in \mathbb{R}^d$ with $d = 1$. Here,

$$\xi = \boldsymbol{V}^{\mathrm{T}} \mathcal{Q}(\boldsymbol{x}), \tag{A1}$$

where $\boldsymbol{V} = (1,\ 0)^{\mathrm{T}}$ and $\boldsymbol{q} = \mathcal{Q}(\boldsymbol{x}) = (\mathcal{Q}_1(\boldsymbol{x}), \mathcal{Q}_2(\boldsymbol{x}))^{\mathrm{T}}$ denotes the projected coordinates. Specifically, we express q_1 and q_2 as polynomials in x_1 and x_2, truncated at quadratic order ($M = 2$),

$$\begin{aligned} q_1 &= \mathcal{Q}_1(\boldsymbol{x}) = p_{11}x_1 + p_{12}x_2 + p_{13}x_1^2 + p_{14}x_1x_2 + p_{15}x_2^2, \\ q_2 &= \mathcal{Q}_2(\boldsymbol{x}) = p_{21}x_1 + p_{22}x_2 + p_{23}x_1^2 + p_{24}x_1x_2 + p_{25}x_2^2. \end{aligned} \tag{A2}$$

We recall that the number of monomials in n variables up to degree M, excluding the constant term, is N_M, with

$$N_M = \binom{n+M}{M} - 1, \tag{A3}$$

and that we have n equations defining the oblique projection, since $\boldsymbol{q} \in \mathbb{R}^n$. The dynamics of the reduced coordinate ξ is also approximated by a polynomial

$$\dot{\xi} = r_1\xi + r_2\xi^2. \tag{A4}$$

In general, this introduces $d\,N_d$ unknown coefficients, with

$$N_d = \binom{d+M}{M} - 1. \tag{A5}$$

Next, we impose that the range of the projection $\mathcal{Q}(\boldsymbol{x})$ lies along $\boldsymbol{V}$, i.e.,

$$\mathcal{Q}(\boldsymbol{x}) = \boldsymbol{V}k(\boldsymbol{x}), \tag{A6}$$

where $k(\boldsymbol{x})$ is a scalar function of $\boldsymbol{x}$, i.e., generically, $k \in \mathbb{R}^d$. We can also expand $k(\boldsymbol{x})$ as a polynomial up to order M,

$$k(\boldsymbol{x}) = k_1x_1 + k_2x_2 + k_3x_1^2 + k_4x_1x_2 + k_5x_2^2. \tag{A7}$$

We note that k_1 and k_2 cannot both be equal to zero, as this would contradict the linearized phase-space decomposition into slow and fast subspaces described in Sec. II A.

The total number of unknowns so far, based on Eqs. (A2)–(A7), is

$$(n + d)N_M + dN_d = 17.$$

By matching the powers of x_1 and x_2 in (A6), we obtain

$$nN_M = 10$$

independent algebraic equations in the unknown coefficients. Imposing the idempotency of the projection,

$$\mathcal{Q}\left(\mathcal{Q}(\boldsymbol{x})\right) = \mathcal{Q}(\boldsymbol{x}),$$

or equivalently

$$k\left(\boldsymbol{V}k(\boldsymbol{x})\right) = k(\boldsymbol{x}), \tag{A8}$$

provides

$$dN_d = 2$$

additional independent equations in the unknown coefficients. In particular, for Example 1, we have

$$\begin{aligned} k_1v_1 + k_2v_2 &= 1, \\ k_3v_1^2 + k_4v_1v_2 + k_5v_2^2 &= 0. \end{aligned} \tag{A9}$$

Considering now the invariance equation of the slow foliation (12) and matching powers of x_1 and x_2, we obtain $dN_M = 5$ further

independent equations in the unknown coefficients. At each order, the number of equations coincides with the number of unknowns. The system can be solved recursively, proceeding in increasing order. At first order, the invariance equations for Example 1 read

$$\begin{aligned} \mathcal{O}(x_1): &\quad -\alpha k_1 = r_1 k_1, \\ \mathcal{O}(x_2): &\quad k_1\delta - k_2\beta = r_1 k_2, \end{aligned} \tag{A10}$$

where we have already used the first-order equations in (A6). Coupling these relations with the first equation in (A9) allows us to uniquely determine r_1, k_1, and k_2. Multiplying the first equation in (A10) by v_1 and the second by v_2, and summing them, we obtain

$$k_1\left(-\alpha v_1 + \delta v_2\right) + k_2\left(-\beta v_2\right) = r_1\left(k_1 v_1 + k_2 v_2\right), \tag{A11}$$

which yields $r_1 = -\alpha$. At this point, we consider the first equation in (A9) together with one equation of (A10). They yield a linear system for k_1 and k_2 that admits a unique solution. Once the first-order coefficients are determined, one can proceed to second order, where the equations form a linear system in the remaining unknowns that can be solved uniquely. In general, after solving the equations at a given order, the next order produces a linear system that can be solved uniquely. Finally, for the SSM parametrization, applying the SSM invariance equation (15) and enforcing tangency of the manifold to $\boldsymbol{V}$ ensure that all terms in the polynomial approximating the SSM are uniquely identified, again by solving linear systems at each order.

APPENDIX B: OPTIMALITY CRITERIA FOR OBLIQUE PROJECTIONS

Identifying the correct direction for the oblique projection, namely, aligning it with the fibers of the slow foliation, amounts to minimizing the rate of convergence between the trajectory of the full system and that of the associated base point. We now demonstrate that recent approaches, such as those by Kogelbauer and Karlin[55] and Buurmeijer *et al.*,[56] which seek the oblique projection that minimizes the deviation between the full and reduced trajectories over time, typically yield a direction that differs from the actual stable fiber directions even in linear examples.

We consider the two-dimensional shear system discussed in Kogelbauer and Karlin,[55]

$$\dot{\boldsymbol{x}} = \boldsymbol{A}\boldsymbol{x}, \quad \boldsymbol{A} = \begin{pmatrix} -1 & \gamma \\ 0 & -\alpha \end{pmatrix}. \tag{B1}$$

Figure 10(a) compares the time series resulting from three projection strategies: orthogonal projection, oblique projection along the direction of the fibers, and the error-minimizing oblique projection. Although the fiber-aligned projection may initially yield a larger projection error, making it suboptimal for minimizing the deviation, it ultimately exhibits the fastest convergence to the full trajectory. Furthermore, as shown in Fig. 10(b), only the fiber-aligned projection accurately captures the geometry of the slow foliation: in particular, the leaf of the foliation passing through the origin coincides with the fast SSM in the fiber-aligned case, whereas it does not under the error-minimizing projection.

APPENDIX C: NON-NORMALITY IN DELAY-EMBEDDED SPACE

Axås and Haller[73] demonstrate that in a delay-embedded observable space, if the linear spectrum is known, one can analytically construct the eigenvectors associated with the known eigenvalues. These eigenvectors are arranged in columns into a Vandermonde matrix $\boldsymbol{V} \in \mathbb{C}^{p\times m}$, where p denotes the number of delays of a scalar observable and m is the number of known modes with

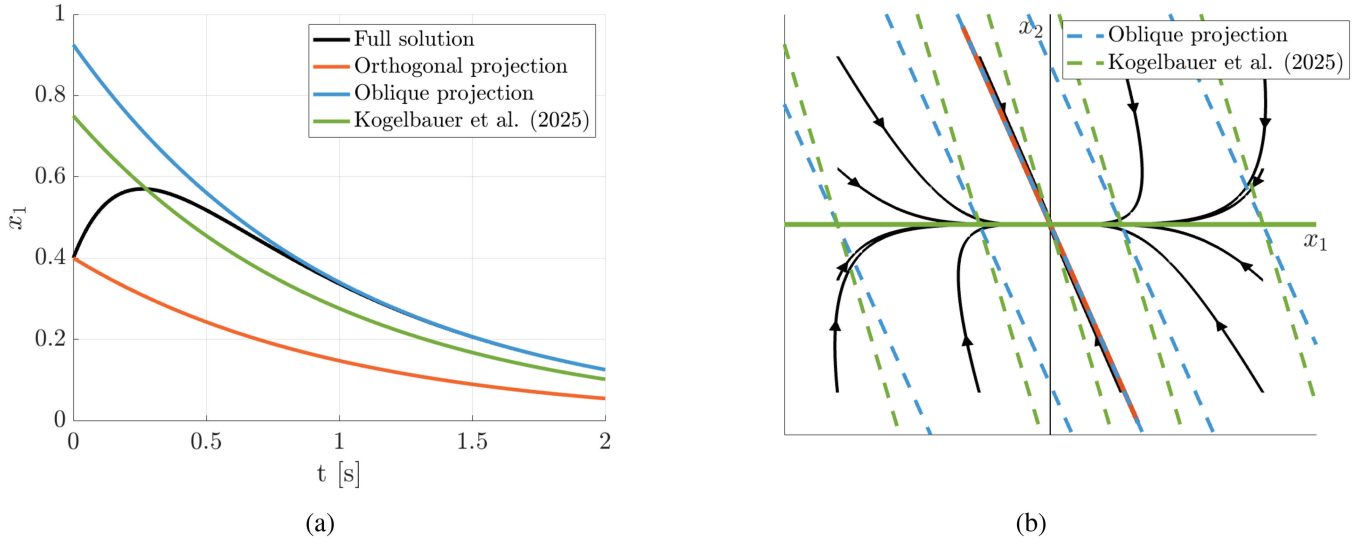

FIG. 10. (a) Time series comparison of different projection strategies for the system (B1). (b) Fiber reconstruction from oblique projections obtained through different strategies. The continuous green line and the dashed red line represent the slow and fast SSMs for the system (B1).

eigenvalues $\lambda_1, \ldots, \lambda_m$. The matrix takes the form

$$V = \begin{pmatrix} 1 & 1 & \cdots & 1 \\ e^{\lambda_1 \tau} & e^{\lambda_2 \tau} & \cdots & e^{\lambda_m \tau} \\ e^{2\lambda_1 \tau} & e^{2\lambda_2 \tau} & \cdots & e^{2\lambda_m \tau} \\ \vdots & \vdots & \ddots & \vdots \\ e^{(p-1)\lambda_1 \tau} & e^{(p-1)\lambda_2 \tau} & \cdots & e^{(p-1)\lambda_m \tau} \end{pmatrix}. \tag{C1}$$

By suitably selecting the number of delays p and the delay time τ, one can minimize the degree of non-normality between spectral subspaces, thereby enabling accurate projection onto spectral subspaces using standard orthogonal projection techniques. However, exact orthogonality among the columns of the Vandermonde matrix $\boldsymbol{V}$ cannot be achieved. Indeed, we observe that $\min(\boldsymbol{V}_i^{\mathrm{T}} \cdot \boldsymbol{V}_j) = 1$ for all i, j, where $\boldsymbol{V}_i$ and $\boldsymbol{V}_j$ denote the columns of $\boldsymbol{V}$. This observation shows that no d-dimensional spectral subspace in the delay-embedded space can be orthogonal to its complementary $(m-d)$-dimensional subspace, making oblique projections essential.

REFERENCES

[1] P. Benner, S. Gugercin, and K. Willcox, "A survey of projection-based model reduction methods for parametric dynamical systems," SIAM Rev. **57**, 483–531 (2015).
[2] C. W. Rowley and S. T. M. Dawson, "Model reduction for flow analysis and control," Annu. Rev. Fluid Mech. **49**, 387–417 (2017).
[3] K. Taira, S. L. Brunton, S. T. Dawson, C. W. Rowley, T. Colonius, B. J. McKeon, O. T. Schmidt, S. Gordeyev, V. Theofilis, and L. S. Ukeiley, "Modal analysis of fluid flows: An overview," AIAA J. **55**, 4013–4041 (2017).
[4] S. L. Brunton, B. R. Noack, and P. Koumoutsakos, "Machine learning for fluid mechanics," Annu. Rev. Fluid Mech. **52**, 477–508 (2020).
[5] A. Ghadami and B. I. Epureanu, "Data-driven prediction in dynamical systems: Recent developments," Philos. Trans. R. Soc. A **380**, 20210213 (2022).
[6] G. Haller, *Modeling Nonlinear Dynamics from Equations and Data—With Applications to Solids, Fluids, and Controls* (Society for Industrial and Applied Mathematics, Philadelphia, PA, 2025).
[7] S. W. Shaw and C. Pierre, "Normal modes for non-linear vibratory systems," J. Sound Vib. **164**, 85–124 (1993).
[8] S. W. Shaw and C. Pierre, "Normal modes of vibration for non-linear continuous systems," J. Sound Vib. **169**, 319–347 (1994).
[9] S. W. Shaw, C. Pierre, and E. Pesheck, "Modal analysis-based reduced-order models for nonlinear structures: An invariant manifold approach," Shock Vib. Dig. **31**, 3–16 (1999).
[10] X. Cabré, E. Fontich, and R. de La Llave, "The parameterization method for invariant manifolds III: Overview and applications," J. Differ. Equ. **218**, 444–515 (2005).
[11] G. Haller and S. Ponsioen, "Nonlinear normal modes and spectral submanifolds: Existence, uniqueness and use in model reduction," Nonlinear Dyn. **86**, 1493–1534 (2016).
[12] S. Wiggins, *Normally Hyperolic Invariant Manifolds in Dynamical Systems* (Springer-Verlag, New York, 1994), Vol. 105.
[13] R. Szalai, "Invariant spectral foliations with applications to model order reduction and synthesis," Nonlinear Dyn. **101**, 2645–2669 (2020).
[14] R. Szalai, "Data-driven reduced order models using invariant foliations, manifolds and autoencoders," J. Nonlinear Sci. **33**, 75 (2023).
[15] L. Bettini, B. Kaszás, B. Zybach, J. Dual, and G. Haller, "Data-driven nonlinear model reduction to spectral submanifolds via oblique projection," Chaos **35**, 043135 (2025).
[16] M. Cenedese, J. Axås, B. Bäuerlein, K. Avila, and G. Haller, "Data-driven modeling and prediction of non-linearizable dynamics via spectral submanifolds," Nat. Commun. **13**, 872 (2022).
[17] M. Cenedese, J. Axås, H. Yang, M. Eriten, and G. Haller, "Data-driven nonlinear model reduction to spectral submanifolds in mechanical systems," Philos. Trans. R. Soc. A **380**, 20210194 (2022).
[18] J. Axås, M. Cenedese, and G. Haller, "Fast data-driven model reduction for nonlinear dynamical systems," Nonlinear Dyn. **111**, 7941–7957 (2023).
[19] M. Cenedese, S. Jain, J. Marconi, and G. Haller, "Data-assisted non-intrusive model reduction for forced nonlinear finite elements models," arXiv:2311.17865 (2023).
[20] G. Haller and R. S. Kaundinya, "Nonlinear model reduction to temporally aperiodic spectral submanifolds," Chaos **34**, 043152 (2024).
[21] L. Bettini, M. Cenedese, and G. Haller, "Model reduction to spectral submanifolds in piecewise smooth dynamical systems," Int. J. Non-Linear Mech. **163**, 104753 (2024).
[22] F. Takens, "Detecting strange attractors in turbulence," in *Dynamical Systems and Turbulence, Warwick 1980*, edited by D. Rand and L.-S. Young (Springer, Berlin, 1981), pp. 366–381.
[23] T. Brack, B. Zybach, F. Balabdaoui, S. Kaufmann, F. Palmegiano, J.-C. Tomasina, S. Blunier, D. Scheiwiller, J. Fankhauser, and J. Dual, "Dynamic measurement of gravitational coupling between resonating beams in the Hertz regime," Nat. Phys. **18**, 952–957 (2022).
[24] L. N. Trefethen, A. E. Trefethen, S. C. Reddy, and T. A. Driscoll, "Hydrodynamic stability without eigenvalues," Science **261**, 578–584 (1993).
[25] P. Schmid and D. Henningson, *Stability and Transition in Shear Flows*, Applied Mathematical Sciences Vol. 142 (Springer-Verlag, 2002).
[26] L. Trefethen and M. Embree, *Spectra and Pseudospectra: The Behavior of Nonnormal Matrices and Operators* (Princeton University Press, 2005).
[27] A. J. Roberts, "Appropriate initial conditions for asymptotic descriptions of the long term evolution of dynamical systems," J. Aust. Math. Soc. Ser. B Appl. Math. **31**, 48–75 (1989).
[28] A. J. Roberts, "Computer algebra derives correct initial conditions for low-dimensional dynamical models," Comput. Phys. Commun. **126**, 187–206 (2000).
[29] P. Holmes, J. L. Lumley, G. Berkooz, and C. W. Rowley, *Turbulence, Coherent Structures, Dynamical Systems and Symmetry*, Cambridge Monographs on Mechanics (Cambridge University Press, 2012).
[30] C. Mullis and R. Roberts, "Synthesis of minimum roundoff noise fixed point digital filters," IEEE Trans. Circuits Syst. **23**, 551–562 (1976).
[31] B. Moore, "Principal component analysis in linear systems: Controllability, observability, and model reduction," IEEE Trans. Autom. Control **26**, 17–32 (1981).
[32] C. W. Rowley, "Model reduction for fluids, using balanced proper orthogonal decomposition," Int. J. Bifurcat. Chaos **15**, 997–1013 (2005).
[33] A. C. Antoulas, "Approximation of large-scale dynamical systems," in *Advances in Design and Control* (SIAM, 2005).
[34] S. Gugercin, A. C. Antoulas, and C. Beattie, "$\mathcal{H}_2$ model reduction for large-scale linear dynamical systems," SIAM J. Matrix Anal. Appl. **30**, 609–638 (2008).
[35] S. Gugercin and A. C. Antoulas, "A survey of model reduction by balanced truncation and some new results," Int. J. Control **77**, 748 (2004).
[36] P. Benner and T. Breiten, *Chapter 6: Model Order Reduction Based on System Balancing: Theory and Algorithms* (Society for Industrial and Applied Mathematics, Philadelphia, PA, 2017), pp. 261–295.
[37] M. Ilak and C. Rowley, "Reduced-order modeling of channel flow using traveling pod and balanced pod," in *Collection of Technical Papers—3rd AIAA Flow Control Conference* (American Institute of Aeronautics and Astronautics Inc., 2006), pp. 864–874.
[38] M. Ilak and C. W. Rowley, "Modeling of transitional channel flow using balanced proper orthogonal decomposition," Phys. Fluids **20**, 034103 (2008).
[39] S. Ahuja and C. Rowley, "Low-dimensional models for feedback stabilization of unstable steady states," in *46th AIAA ASME* (American Institute of Aeronautics and Astronautics, 2008).
[40] S. Bagheri, L. Brandt, and D. Henningson, "Input–output analysis, model reduction and control of the flat-plate boundary layer," J. Fluid Mech. **620**, 263–298 (2009).
[41] A. Barbagallo, D. Sipp, and P. J. Schmid, "Closed-loop control of an open cavity flow using reduced-order models," J. Fluid Mech. **641**, 1–50 (2009).
[42] J. M. A. Scherpen, "Balancing for nonlinear systems," Syst. Control Lett. **21**, 143–153 (1993).

[43]J. M. A. Scherpen and A. J. Van der Schaft, "Normalized coprime factorizations and balancing for unstable nonlinear systems," Int. J. Control **60**, 1193–1222 (1994).
[44]W. Gray and J. Scherpen, "On the nonuniqueness of singular value functions in balanced nonlinear realizations," in *Proceedings of the 1999 Conference on Information Sciences and Systems* (University of Gröningen, Research Institute of Technology and Management, 1999), pp. 729–734.
[45]K. Fujimoto and D. Tsubakino, "Computation of nonlinear balanced realization and model reduction based on Taylor series expansion," Syst. Control Lett. **57**, 283–289 (2008).
[46]B. Kramer, S. Gugercin, and J. Borggaard, "Nonlinear balanced truncation: Part 1—Computing energy functions," arXiv.2209.07645 (2022).
[47]B. Kramer, S. Gugercin, and J. Borggaard, "Nonlinear balanced truncation: Part 2—Model reduction on manifolds," arXiv.2302.02036 (2023).
[48]S. E. Otto, A. Padovan, and C. W. Rowley, "Model reduction for nonlinear systems by balanced truncation of state and gradient covariance," SIAM J. Sci. Comput. **45**, A2325–A2355 (2023).
[49]S. E. Otto, G. R. Macchio, and C. W. Rowley, "Learning nonlinear projections for reduced-order modeling of dynamical systems using constrained autoencoders," Chaos **33**, 113130 (2023).
[50]S. Ahuja and C. W. Rowley, "Feedback control of unstable steady states of flow past a flat plate using reduced-order estimators," J. Fluid Mech. **645**, 447–478 (2010).
[51]S. J. Illingworth, A. S. Morgans, and C. W. Rowley, "Feedback control of flow resonances using balanced reduced-order models," J. Sound Vib. **330**, 1567–1581 (2011).
[52]P. Benner, P. Goyal, and S. Gugercin, "$\mathcal{H}_2$-quasi-optimal model order reduction for quadratic-bilinear control systems," SIAM J. Matrix Anal. Appl. **39**, 983–1032 (2018).
[53]S. E. Otto, A. Padovan, and C. W. Rowley, "Optimizing oblique projections for nonlinear systems using trajectories," SIAM J. Sci. Comput. **44**, A1681–A1702 (2022).
[54]G. Haller and B. Kaszás, "Data-driven linearization of dynamical systems," Nonlinear Dyn. **112**, 18639–18663 (2024).
[55]F. Kogelbauer and I. Karlin, "Dynamically optimal projection onto slow spectral manifolds for linear systems," arXiv.2503.18021 (2025).
[56]H. Buurmeijer, L. A. Pabon, J. I. Alora, R. S. Kaundinya, G. Haller, and M. Pavone, "Taming high-dimensional dynamics: Learning optimal projections onto spectral submanifolds," arXiv:2504.03157 (2025).
[57]S. Sternberg, "Local contractions and a theorem of poincare," Am. J. Math. **79**, 809–824 (1957).
[58]S. Banerjee and A. Roy, *Linear Algebra and Matrix Analysis for Statistics*, 1st ed. (Chapman and Hall/CRC, 2014).
[59]K. Champion, B. Lusch, J. N. Kutz, and S. L. Brunton, "Data-driven discovery of coordinates and governing equations," Proc. Natl. Acad. Sci. U.S.A. **116**, 22445–22451 (2019).
[60]A. Padovan, B. Vollmer, and D. J. Bodony, "Data-driven model reduction via non-intrusive optimization of projection operators and reduced-order dynamics," SIAM J. Appl. Dyn. Syst. **23**, 3052 (2024).
[61]H. Whitney, "The self-intersections of a smooth n-manifold in $2n$-space," Ann. Math. **45**, 220–246 (1944).
[62]C. G. Broyden, "The convergence of a class of double-rank minimization algorithms 1. General considerations," IMA J. Appl. Math. **6**, 76–90 (1970).
[63]R. Fletcher, "A new approach to variable metric algorithms," Comput. J. **13**, 317–322 (1970).
[64]D. Goldfarb, "A family of variable-metric methods derived by variational means," Math. Comput. **24**, 23–26 (1970).
[65]D. F. Shanno, "Conditioning of quasi-Newton methods for function minimization," Math. Comput. **24**, 647–656 (1970).
[66]B. Fornberg, "Generation of finite difference formulas on arbitrarily spaced grids," Math. Comput. **51**, 699 (1988).
[67]B. Noack, K. Afanasiev, M. Morzynski, G. Tadmor, and F. Thiele, "A hierarchy of low-dimensional models for the transient and post-transient cylinder wake," J. Fluid Mech. **497**, 335–363 (2003).
[68]M. Jin, W. Chen, M. R. W. Brake, and H. Song, "Identification of instantaneous frequency and damping from transient decay data," J. Vib. Acoust. **142**, 051111 (2020).
[69]E. Acome, S. K. Mitchell, T. G. Morrissey, M. B. Emmett, C. Benjamin, M. King, M. Radakovitz, and C. Keplinger, "Hydraulically amplified self-healing electrostatic actuators with muscle-like performance," Science **359**, 61–65 (2018).
[70]T. J. K. Buchner, T. Fukushima, A. Kazemipour, S.-D. Gravert, M. Prairie, P. Romanescu, P. Arm, Y. Zhang, X. Wang, S. L. Zhang, J. Walter, C. Keplinger, and R. K. Katzschmann, "Electrohydraulic musculoskeletal robotic leg for agile, adaptive, yet energy-efficient locomotion," Nat. Commun. **15**, 7634 (2024).
[71]S.-D. Gravert, E. Varini, A. Kazemipour, M. Y. Michelis, T. Buchner, R. Hinchet, and R. K. Katzschmann, "Low-voltage electrohydraulic actuators for untethered robotics," Sci. Adv. **10**, 1 (2024).
[72]L. Bettini, A. Kazemipour, R. K. Katzschmann, and G. Haller, "Data-driven modeling of artificial muscles for soft robot control," preprint, arXiv:2601.03247v1 (2025).
[73]J. Axås and G. Haller, "Model reduction for nonlinearizable dynamics via delay-embedded spectral submanifolds," Nonlinear Dyn. **111**, 22079–22099 (2023).
[74]L. Bettini, A. Kazemipour, R. K. Katzschmann, and G. Haller (2026). "MATLAB code for data-driven SSM with general oblique projection," see https://github.com/haller-group/SSMLearn.